LASER & PHOTONICS REVIEWS

www.lpr-journal.org

Transverse-Electric-Polarized Polaritons Propagating in a $WS_2/Si_3N_4/Ag$ Heterostructure

*Shulei Li, Lidan Zhou, Fu Deng, Jin Xiang, Mingcheng Panmai, Hongxing Huang, Guangcan Li, Jingdong Chen, and Sheng Lan**

Strong light–matter interaction has attracted great interest due to its potential applications in photonic and plasmonic devices. So far, many studies focus on micro- and nanocavities with three-dimensional confinement of light. Here, we investigate the coupling between the surface waves supported by a dielectric-metal heterostructure and the excitons in a two-dimensional material. It is revealed that the transverse-electric (TE) polarized waves excited in the dielectric-metal heterostructure possess significantly enhanced in-plane electric field on the surface of the dielectric layer. This unique property makes it possible to realize strong photon–exciton coupling with the excitons in a two-dimensional material. By using a tungsten disulfide (WS_2)/silicon nitride (Si_3N_4)/silver (Ag) heterostructure, we demonstrate the strong coupling of the TE polarized waves with the two excitons (both A and B excitons) in the WS_2 monolayer, creating TE polarized polaritons propagating in the heterostructure. The strong photon–exciton coupling is revealed in the angle-resolved reflection or scattering spectra with a Rabi splitting larger than the average damping rate of the TE polarized wave and the exciton.
Our findings open new horizons for manipulating light–matter interaction in two-dimensional nanostructures and indicate the potential applications of such propagating polaritons in photonic and plasmonic devices.

1. Introduction

The interaction between light and matter has always been a research hotspot in the field of modern optics. It is well known that strong photon–exciton coupling characterized by a large Rabi splitting can be realized if the energy exchange rate between them exceeds their average damping rate, leading to the formation of hybrid states with part-light and part-matter characteristics.[1,2] Strong coupling between photons and excitons has exhibited great advantages in many practical applications such as quantum manipulation,[3,4] ultrafast switching,[5,6] and low-threshold laser.[7–9] In general, strong localization of light, which is available in optical cavities, is necessary for the realization of strong photon–exciton coupling. In addition, organic molecules or quantum dots with sharply defined exciton resonances are usually used in photon–exciton coupling.[10,11] An alternative to the localization of light can be achieved by utilizing surface plasmon resonances (SPRs) supported by metallic nanoparticles/nanostructures and surface plasmon polaritons (SPPs) propagating on the surfaces of metal films, which can be employed to realize strong plasmon–exciton coupling.[12,13] Particularly, the excitonic system can be incorporated in a convenient open planar geometry in the latter case, making it possible to achieve propagating mixed states, referred to as plexcitons.[14–16] Basically, SPPs can be generated on the surface of a metal film by using the so-called Kretschmann–Raether configuration,[17]

S. Li, L. Zhou, M. Panmai, H. Huang, G. Li, S. Lan
Guangdong Provincial Key Laboratory of Nanophotonic Functional Materials and Devices, School of Information and Optoelectronic Science and Engineering
South China Normal University
Guangzhou 510006, P. R. China
E-mail: slan@scnu.edu.cn

S. Li
School of Optoelectronic Engineering
Guangdong Polytechnic Normal University
Guangzhou 510665, P. R. China

L. Zhou
State Key Laboratory of Optoelectronic Materials and Technologies | School of Electronics and Information Technology
Sun Yat-sen University
No. 135, Xingang Xi Road, Guangzhou, Guangdong 510275, P. R. China

F. Deng
Department of Physics
The Hong Kong University of Science and Technology
Clear Water Bay, Kowloon, Hong Kong 999077, P. R. China

J. Xiang
Key Laboratory of Optoelectronic Technology and Systems (Chongqing University), Ministry of Education, School of Optoelectronic Engineering
Chongqing University
Chongqing 400044, P. R. China

J. Chen
College of Physics and Information Engineering
Minnan Normal University
Zhangzhou 363000, P. R. China

The ORCID identification number(s) for the author(s) of this article can be found under https://doi.org/10.1002/lpor.202100457

DOI: 10.1002/lpor.202100457

creating transverse and longitudinal electric fields that are localized on the surface of the metal film.[18] Although strong plasmon–exciton coupling has been successfully demonstrated in a hybrid system composed of a 2D material and a thin metal film,[19–21] the large Ohmic loss of metals in the visible light spectrum leads to low quality factor and serious propagation loss for SPPs, which strongly limit the plasmon–exciton coupling strength and its applications in practical devices.

In recent years, transition metal dichalcogenides (TMDCs) have attracted great interest because the excitons in such materials generally possess large binding energies and dipole moments, offering us the opportunity for studying strong plasmon–exciton coupling at room temperature.[22–25] Recently, the strong coupling between the excitons in TMDC monolayers and the optical/plasmonic modes supported by various resonators has been realized, including optical microcavities and metallic nanoparticle arrays.[26–29] At the single nanoparticle level, the strong coupling of TMDC monolayers with various plasmonic nanoparticles has been successfully demonstrated.[30,31] Due to the small mode volumes of plasmonic resonators and the large transition dipole moments of TMDC monolayers, a Rabi splitting of 80–120 meV can be achieved.[32,33] To further enhance light–matter interaction, particle-on-film systems with embedded TMDC monolayers are employed, increasing Rabi splitting to 120–170 meV.[34,35] So far, the most popular TMDCs commonly used in the study of strong plasmon–exciton coupling are WS_2 and MoS_2, which possess an optical absorption as large as 10–15% for monolayer.[36] Both of them have two exciton resonances of particular interest in the visible light spectrum, which are generally referred to as A and B excitons (X_A and X_B).[37] In most cases, strong plasmon–exciton coupling is demonstrated by using X_A because the dipole moment of X_B is much smaller, especially in the case of monolayer. Since the coupling strength can be enhanced by increasing the number of excitons involved in the coupling, it was found that strong coupling between the SPPs excited on the surface of a thin Ag film and the two excitons in MoS_2 can be simultaneously observed when few-layer MoS_2 was employed, leading to the hybridization of the two exciton resonances.[38]

Physically, the formation of mixed states or the appearance of energy splitting appears at the quantum exceptional point (QEP) where the critical coupling strength is given by $g_{QEP} = |\gamma_{pl} - \gamma_{ex}|/4$.[39–41] It is apparent that energy splitting and strong photon–exciton or plasmon–exciton coupling can be easily realized when the damping rate of photons or plasmons is close to that of excitons. Basically, the damping rates of photons/plasmons and excitons are characterized by their linewidths. The linewidth of the exciton resonance in WS_2 monolayer is ≈10 nm, which is much smaller as compared with the linewidth of SPPs (≈60 nm). The large difference between them makes it difficult to achieve strong coupling between SPPs and excitons. For this reason, the realization of the strong coupling between the SPPs and the excitons in WS_2 monolayer was mediated by Ga nanoparticles.[21] Otherwise, few-layer MoS_2 must be used to observe the strong SPP–exciton coupling,[38] as mentioned above.

Very recently, we revealed that transverse-electric (TE) polarized waves, being the counterparts of SPPs (i.e., transverse-magnetic (TM) polarized waves), can be excited in a dielectric-metal heterostructure by exploiting the so-called optical magnetism.[42,43] In sharp contrast to SPPs, such TE-polarized waves possess narrow linewidths or small damping rates due to the spatial separation between the electric and magnetic fields. More importantly, they have only the in-plane electric field component, which is strongly localized on the surface of the dielectric layer. This unique feature makes them very attractive for realizing strong coupling with the excitons in a 2D material, which can be easily attached on the surface of the dielectric layer. Similar to SPPs, the resonant wavelength of a TE wave can be readily tuned by simply varying the incidence angle of the excitation light.

In this article, we proposed a semiconductor–dielectric-metal hybrid nanostructure consisting of a WS_2 monolayer attached on a silicon nitride (Si_3N_4)/silver (Ag) heterostructure and demonstrated numerically and experimentally the realization of the strong coupling between the lowest-order TE wave propagating in the heterostructure and the two excitons (X_A and X_B) in the WS_2 monolayer simultaneously. It was revealed that the enhanced in-plane electric field and reduced damping rate achieved in the TE wave play a crucial role in the realization of strong photon–exciton coupling. The strong coupling was reflected in the anti-crossing behavior in the angle-resolved reflection and scattering spectra, and confirmed by the large Rabi splitting of ≈130.1 meV for X_A and ≈144.9 meV for X_B.

2. Results and Discussion

Being TM waves, SPPs propagating on the surface of a bare metal film (or the interface between air and metal) can only be excited by using *p*-polarized light because the longitudinal electric field (E_x) can be created by exploiting the collective oscillation of electrons in the metal film. However, a TE wave is not supported on the surface of a bare metal film because there is no analytical solution to the Maxwell equation. Very recently, it was found that such a TE wave becomes available in a dielectric-metal heterostructure formed by adding a thin dielectric film on the metal film, which can be interpreted in terms of optical magnetism.[42] The most intriguing feature of the TE wave is the spatial separation of the electric (E_y) and magnetic (H_x and H_z) fields, which are located on the surfaces of the dielectric film and the metal film, respectively (see Figure S1 in the Supporting Information). In this work, this unique feature of the TE wave (i.e., the strong localization of the electric field on the surface of the dielectric film) is employed to realize strong coupling simultaneously with the two exciton resonances of WS_2 monolayer.

In **Figure 1**a, we show schematically the TE waves excited in a heterostructure composed of a 100 nm thick Si_3N_4 layer and a 50 nm thick Ag film deposited on a silica (SiO_2) substrate. Physically, the TE waves supported by the Si_3N_4/Ag heterostructure belong to substrate-modulated waveguide modes because their resonant wavelengths are quite sensitive to the thickness of the dielectric layer (see Figure S2 in the Supporting Information), similar to those described in a previous study where a polaritonic substrate was employed.[44] They can only be excited by using evanescent wave (see Figure S3 in the Supporting Information). The resonant wavelength of the lowest-order TE wave can be adjusted in the visible spectrum by simply varying the incidence angle of the excitation white light (*s*-polarized), as shown in Figure 1b. In this way, the resonant wavelength of a TE wave can be tuned in the

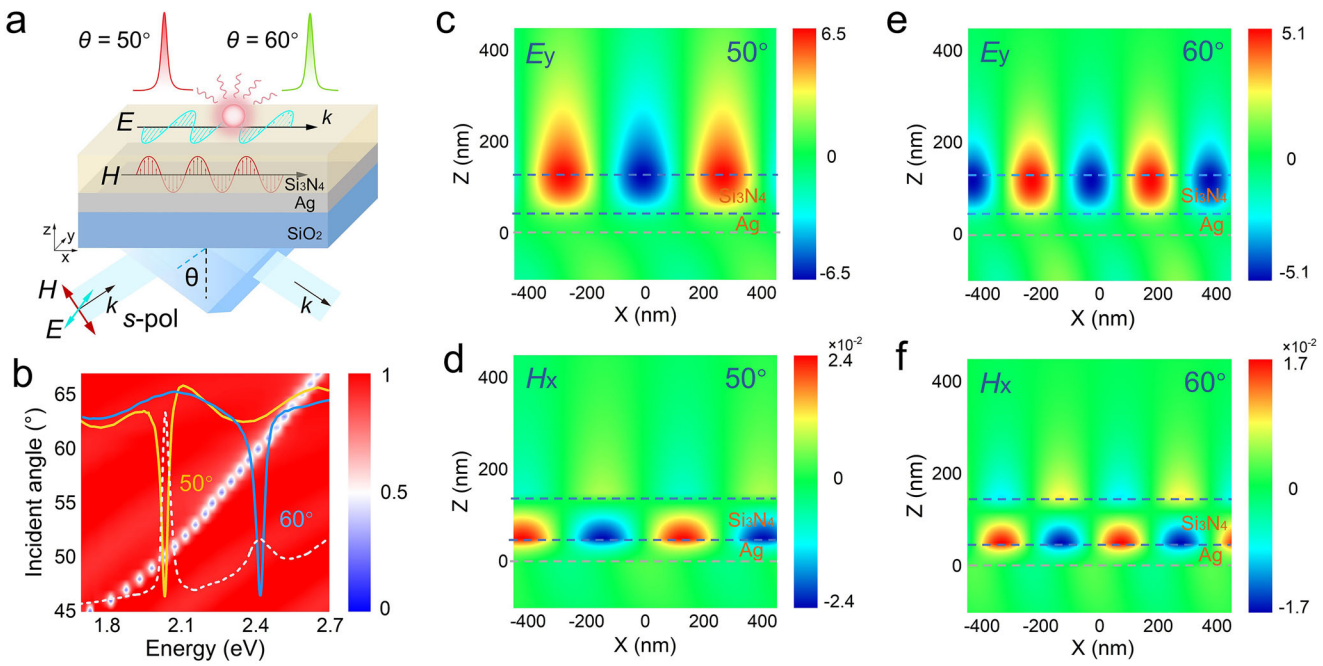

Figure 1. a) Schematic showing the excitation of TE waves in a Si_3N_4/Ag and a WS_2/Si_3N_4/Ag heterostructure by using *s*-polarized white light and the extraction of TE waves by using a PS nanoparticle. b) Dependence of the resonant wavelength of the TE wave on the incidence angle of the excitation light calculated for a Si_3N_4/Ag heterostructure with h = 100 nm. The imaginary part of the dielectric constant of WS_2 monolayer, from which the two excitons (X_A and X_B) can be identified, is shown by a dotted curve. The reflection spectra obtained at 49° and 59° are presented by using yellow and blue curves, respectively. c,d) The E_y and H_x components calculated for the TE wave at an incidence angles of 50°. e,f) The E_y and H_x components calculated for the TE wave at an incidence angles of 60°.

spectral range of 1.7–2.7 eV across the two exciton resonances of the WS_2 monolayer, which are located at 2.02 eV (X_A) and 2.41 eV (X_B), respectively. In Figure 1b, we also presented the reflection spectra obtained at two incidence angles of 50° and 60°, where the TE waves resonant with the two exciton resonances are excited. The linewidths of the two reflection dips, which reflect the damping rates of the TE waves, are found to be ≈36 and ≈56 meV. These values are much smaller than those of the TM waves at the same energies (≈190 and ≈230 meV) but comparable to those of the two exciton resonances (≈33 and ≈80 meV). As mentioned above, the comparable damping rates of the TE waves and the two exciton resonances lead to a small value for the critical coupling strength, implying that the strong coupling between the TE waves and the exciton resonances can be easily realized. In Figure 1c,e, we present the electric field distributions calculated for the TE waves generated at the two incidence angles (50° and 60°). The corresponding magnetic field distributions are shown in Figure 1d,f. In both cases, it is remarkable that the electric field is localized on the surface of the Si_3N_4 layer, and the magnetic field is localized at the interface between the Si_3N_4 layer and the Ag film. This behavior is completely different from that observed for the TM wave, whose electric and magnetic fields are localized on the surface of the Ag film. It has been known that the separation of electric and magnetic fields in a photonic crystal leads to a small group velocity or the strong localization of electromagnetic wave.[45,46] This unique feature of the TE wave renders it a high quality factor or a narrow linewidth. In addition, the TE wave is a propagating wave in the Si_3N_4 layer with negligible radiation loss (see Figure S4 in the Supporting Information).

More importantly, the in-plane electric field (E_y) of the TE wave, which is crucial for the coupling of the TE wave with the excitons in the WS_2 monolayer, is enhanced by a factor of ≈3.0 as compared with the corresponding TW wave (E_x) (see Figure S5 in the Supporting Information). Therefore, a stronger plasmon–exciton coupling is anticipated for the TE wave and the WS_2 monolayer in the WS_2/Si_3N_4/Ag heterostructure, as demonstrated later.

Basically, WS_2 is a semiconductor with its bandgap energy spanning the visible to near-infrared spectral range, and its optical properties are dominated by excited electron–hole pairs, i.e., excitons. As mentioned above, coupling between the TE wave and the excitons excited in the WS_2 monolayer can be realized by simply changing the incidence angle. Basically, we can use a Hamiltonian, which is expressed as follows, to describe the plasmon–exciton coupling[19,47,48]

$$\begin{pmatrix} E_{TE} - i\hbar\gamma_{TE} & g \\ g & E_{ex} - i\hbar\gamma_{ex} \end{pmatrix} \begin{pmatrix} \alpha \\ \beta \end{pmatrix} = E_{\pm} \begin{pmatrix} \alpha \\ \beta \end{pmatrix} \quad (1)$$

Here E_{TE} and E_{ex} are the resonant energies of the TE wave and excitons, γ_{TE} and γ_{ex} are the corresponding damping rates, g is the coupling strength, $E_{\pm}$ are the eigenenergies of the hybrid states, and α and β are the eigenparameters satisfying $|\alpha|^2 + |\beta|^2 = 1$. The eigenenergies $E_{\pm}$ can be derived as follows

$$E_{\pm} = \frac{E_{TE} + E_{ex}}{2} \pm \frac{\sqrt{4g^2 + (\delta - \frac{i}{2}(\gamma_{TE} - \gamma_{ex}))^2}}{2} \quad (2)$$

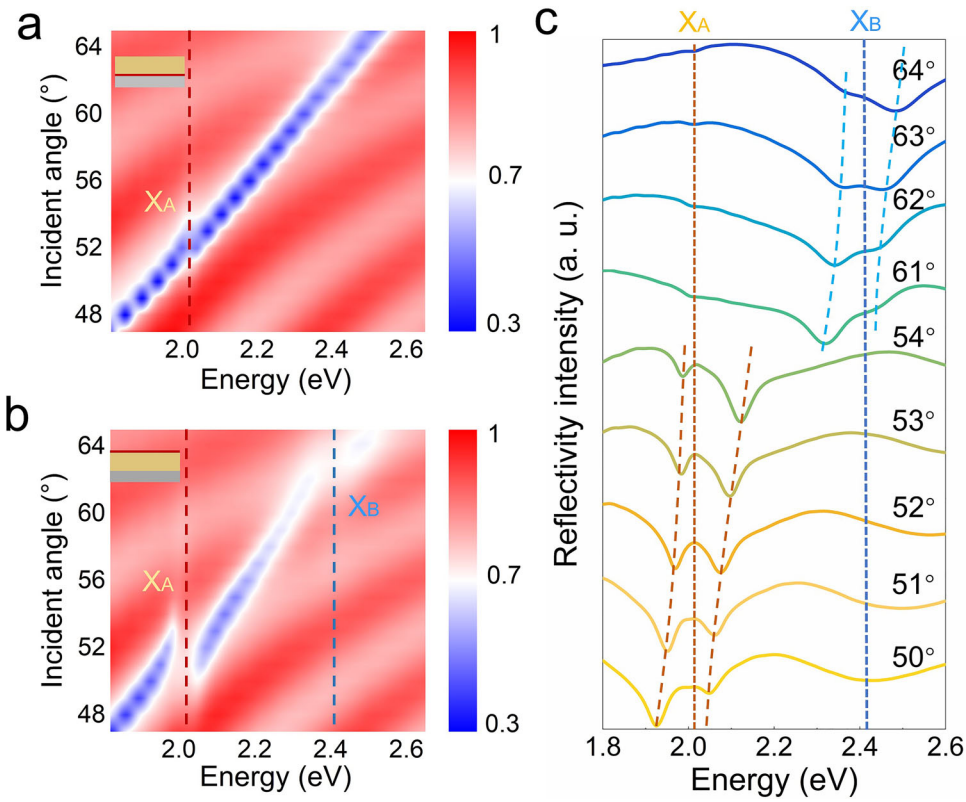

Figure 2. 2D reflectivity calculated for a) a $Si_3N_4/WS_2/Ag$ and b) a $WS_2/Si_3N_4/Ag$ heterostructure excited by using *s*-polarized white light with different incidence angles. c) The reflection spectra obtained for the $WS_2/Si_3N_4/Ag$ heterostructure at different incidence angles.

where $\delta = E_{TE} - E_{ex}$ is the detuning energy. When the TE wave is resonant with the exciton resonance (i.e., $\delta = 0$), the Rabi splitting energy $\hbar\Omega$ is given by

$$\hbar\Omega = \sqrt{4g^2 - \frac{(\gamma_{TE} - \gamma_{ex})^2}{4}} \tag{3}$$

In this case, the critical coupling strength at QEP can be obtained by setting $\hbar\Omega = 0$

$$g_{QEP} = \frac{|\gamma_{TE} - \gamma_{ex}|}{4} \tag{4}$$

Physically, the energy level is no longer degenerated but is split into two parts when $g > g_{QEP}$. According to Equation (3), a smaller g_{QEP} will result in a larger $\hbar\Omega$ for a specific g (see Figure S6 in the Supporting Information). It implies that it is easier for a system with a small g_{QEP} to enter into the strong coupling regime, in which the following criterion is satisfied

$$\hbar\Omega > \frac{\gamma_{TE} + \gamma_{ex}}{2} \tag{5}$$

Based on the damping rates extracted for the TE waves at the two exciton resonances ($\gamma_{TE}^{A} \approx 36$ meV and $\gamma_{TE}^{B} \approx 56$ meV) and the damping rates reported previously for the two excitons in WS_2 monolayer ($\gamma_A \approx 33$ meV for X_A and $\gamma_B \approx 80$ meV for X_B), we can easily derive $g_{QEP}^{A} \approx 0.75$ meV and $g_{QEP}^{B} \approx 6.0$ meV. The small g_{QEP} for both excitons implies that it is easy to observe energy level splitting and to realize strong coupling.

Now we examine the coupling of the TE waves excited at 50° and 60° with X_A and X_B exciton resonances being in the WS_2 monolayer by using numerical simulation. In order to confirm the localization of the electric field on the Si_3N_4 layer, we intentionally placed the WS_2 monolayer in between the Ag film and the Si_3N_4 layer, as schematically shown in the inset of **Figure 2**a. Previously, it was shown that the coupling between the TM wave and a WS_2 monolayer can be enhanced by covering the WS_2 monolayer with a dielectric layer having a large dielectric constant.[49] In Figure 2a, we show the 2D reflection spectra simulated for the $Si_3N_4/WS_2/Ag$ heterostructure excited by using *s*-polarized light with different incidence angles. It is found that the continuous dispersion curve of the TE wave is weakly disturbed only at X_A resonance (see Figure S7 in the Supporting Information). This phenomenon indicates that the electric field of the TE wave is quite weak at the interface between the Si_3N_4 layer and the Ag film, and the dipole moment of X_B is much weaker as compared with that of X_A.

In the $WS_2/Si_3N_4/Ag$ heterostructure, the reflection spectra are modified due to the interaction of the three modes, i.e., the TE wave, the A exciton, and the B exciton, as shown in Figure 2b. We present the 2D reflection spectra simulated for the $WS_2/Si_3N_4/Ag$ heterostructure when the polarization angle of the *s*-polarized light is changed from 45° to 65°. In sharp contrast, one can clearly identify the anticrossing behaviors appearing at the two exciton resonances, implying the existence of

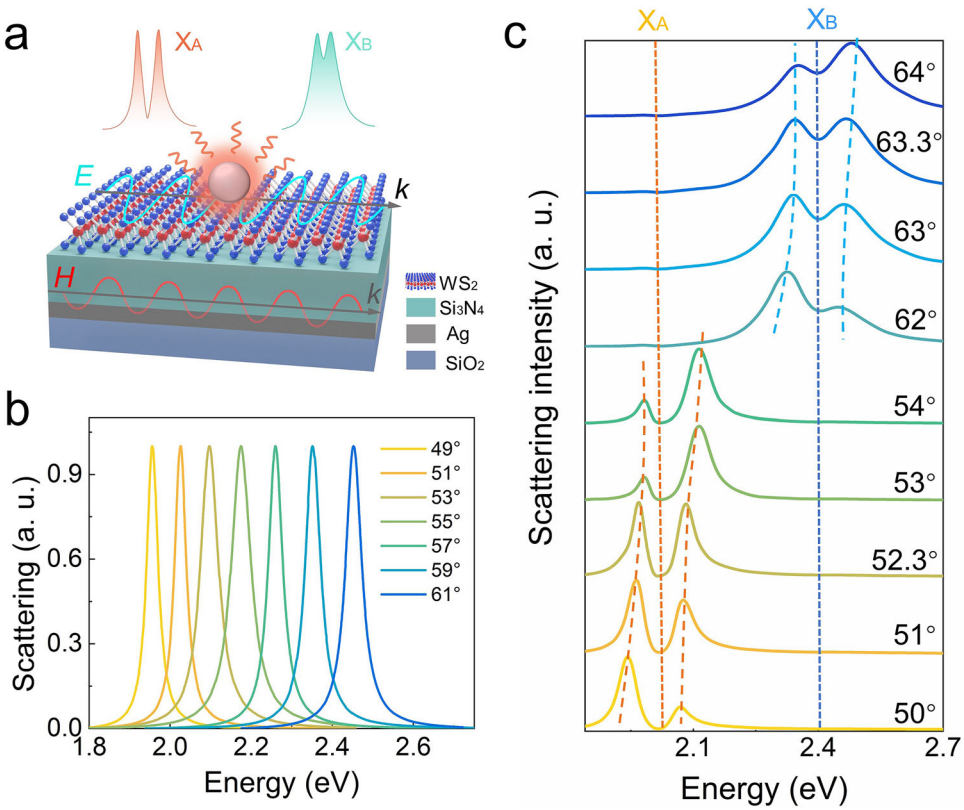

Figure 3. a) Schematic showing the excitation of TE waves in a Si_3N_4/Ag and a WS_2/Si_3N_4/Ag heterostructure by using *s*-polarized white light and the extraction of TE waves by using a PS nanoparticle. b) Simulated scattering spectra for the PS nanoparticle excited by using the TE waves generated with *s*-polarized white light at different incidence angles. c) Simulated scattering spectra for the PS nanoparticle placed on the WS_2/Si_3N_4/Ag heterostructure.

photon–exciton coupling. Similarly, the dependences of the resonant energies of the three hybrid states on the resonant energy of the TE wave can be described by using a Hamiltonian with three eigenvalues based on the coupled harmonic oscillator model, which is expressed as follows

$$\hat{H} = \hbar \begin{pmatrix} E_{\mathrm{TE}} - \mathrm{i}\frac{\gamma_{\mathrm{TE}}}{2} & g_{\mathrm{TE-ex_B}} & g_{\mathrm{TE-ex_A}} \\ g_{\mathrm{TE-ex_B}} & E_{\mathrm{ex}}^{\mathrm{B}} - \mathrm{i}\frac{\gamma_{\mathrm{ex}}^{\mathrm{B}}}{2} & 0 \\ g_{\mathrm{TE-ex_A}} & 0 & E_{\mathrm{ex}}^{\mathrm{A}} - \mathrm{i}\frac{\gamma_{\mathrm{ex}}^{\mathrm{A}}}{2} \end{pmatrix} \tag{6}$$

Here, E_{TE}, $E_{\mathrm{ex}}^{\mathrm{A}}$, and $E_{\mathrm{ex}}^{\mathrm{B}}$ are the resonant energies of the uncoupled TE wave and the two (A and B) exciton modes; γ_{TE}, $\gamma_{\mathrm{ex}}^{\mathrm{A}}$, and $\gamma_{\mathrm{ex}}^{\mathrm{B}}$ are the corresponding dissipation rates; $g_{\mathrm{TE-ex_A}}$, $g_{\mathrm{TE-ex_B}}$, and $g_{\mathrm{ex_A-ex_B}}$ are the coupling strengths between the TE wave and the A exciton, that between the TE wave and the B exciton, and that between the A exciton and the B exciton. Since the two exciton resonances are well separated, we have $g_{\mathrm{ex_A-ex_B}} = 0$. For clarity, the reflection spectra obtained at several incidence angles around $\theta = 52°$ (X_A) and 63° (X_B), where the energy of the TE wave coincides with the exciton energies (≈2.02 and ≈2.41 eV), are presented in Figure 2c. The energy splitting values extracted from the reflection spectra at zero detuning energy are found to be ≈106.2 meV (TE-X_A), ≈119.5 meV (TE-X_B), and 0 meV (X_A–X_B) in the three-component system (TE-X_A–X_B). There is no coupling between the two exciton resonances because they are well separated. The Rabi splitting energies observed for the TE wave at the two exciton resonances are much larger than those observed for the TM wave propagating on the surface of the Ag film (see Figure S8 in the Supporting Information). Apparently, the criterion for strong coupling is fulfilled (i.e., $\hbar\Omega > |\gamma_{\mathrm{TE}} \pm \gamma_{\mathrm{ex}}|/2$), indicating that the photon–exciton coupling in both cases enters undoubtedly into the strong-coupling regime.

In order to confirm experimentally the strong photon–exciton coupling predicted for the WS_2/Si_3N_4/Ag heterostructure, we need to measure the angle-resolved reflection spectra from which the energy splitting can be extracted. However, it remains a big challenge to carry out such a measurement because of the availability of a WS_2 monolayer with a large size (larger than the diameter of the incident white light) and the difficulty of transferring it to the Si_3N_4/Ag heterostructure. As an alternative, we employed a polystyrene (PS) nanoparticle with a diameter of ≈300 nm on the WS_2 monolayer as the scatter for the TE wave, as schematically shown in **Figure 3**a. Such a PS nanoparticle (with a low refractive index of ≈1.5) does not have any optical resonance in the visible light spectrum, which may lead to the enhancement of the local electric field. As a result, the TE wave propagating in the heterostructure can be perfectly extracted by utilizing the scattering spectrum of the PS nanoparticle. In Figure 3b, we show the simulated scattering spectra for the PS nanoparticle placed on the Si_3N_4/Ag heterostructure. Here, the linewidth of the TE wave obtained in the scattering spectra is very close to that

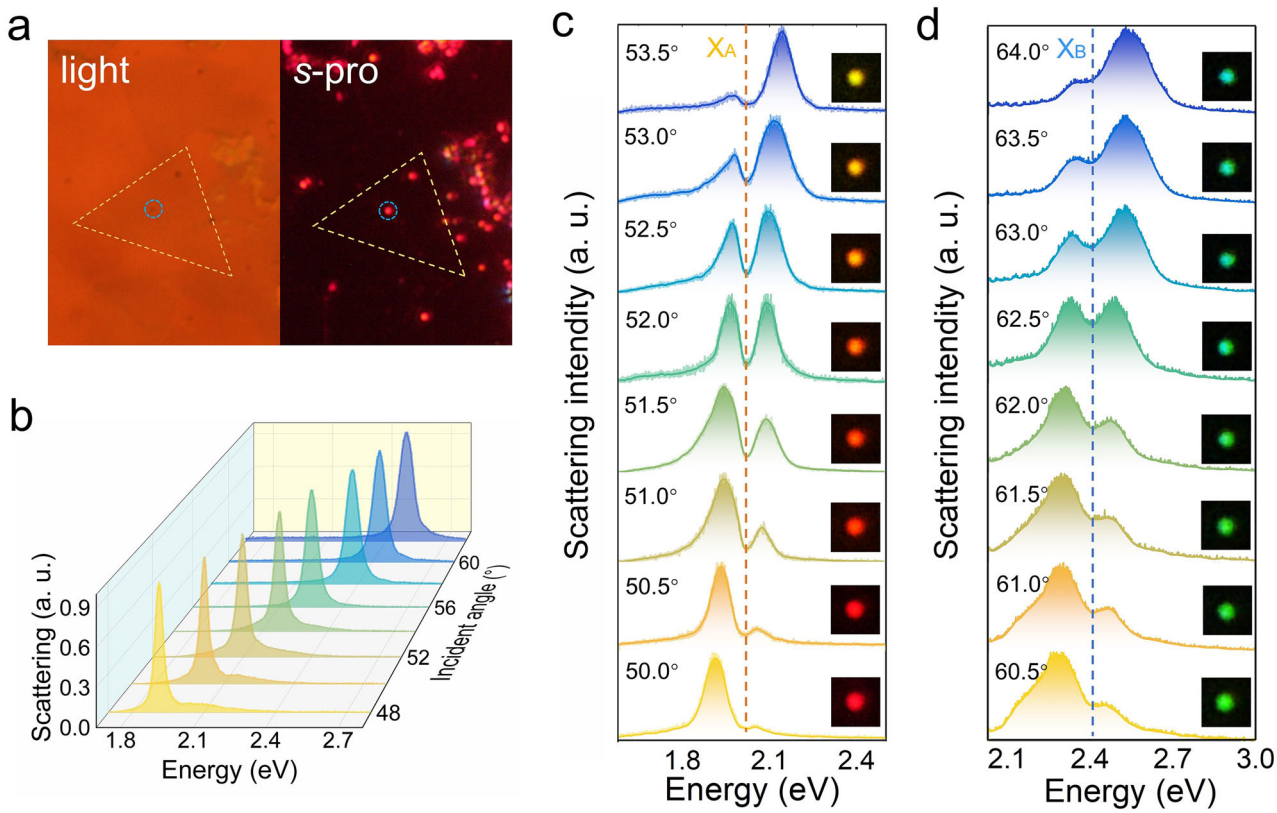

Figure 4. a) Bright- and dark-field images of a WS_2 monolayer attached on a Si_3N_4/Ag heterostructure. The PS nanoparticle located on the WS_2 monolayer, which is used as the scatter for TE waves, is enclosed by a circle. b) Measured scattering spectra for the PS nanoparticle placed on the Si_3N_4/Ag heterostructure and excited using *s*-polarized white light at different incidence angles. Measured scattering spectra for the PS nanoparticle placed on the WS_2/Si_3N_4/Ag heterostructure and excited by using *s*-polarized white light at different incidence angles ranging from c) 50.0° to 53.5° and from d) 60.5° to 64.0°. In each case, the CCD images of the scattering light are shown as insets.

observed in the reflection spectra, implying that the damping rate of the TE wave remains almost unchanged. We calculated the angle-resolved scattering spectra for the PS nanoparticle, which is excited by the TE wave generated by using *s*-polarized light with different incidence angles, as shown in Figure 3c. As expected, anticrossing behaviors are also revealed at the two exciton resonances, implying the feasibility of this method. In this case, a nanocavity with a large mode volume is created. Thus, the excitons would feel a slightly enhanced electric field as compared with the TE wave (see Figure S9 in the Supporting Information). Consequently, we observed larger values of energy splitting for the two excitons (≈120.2 meV for X_A and ≈139.7 meV for X_B). We also examined the evolution of the in-plane electric field, which is localized on the surface of the Si_3N_4 layer, when the energy of the TE wave sweeps the exciton resonances through the variation of the incidence angle. It indicates clearly that the energy of the system, which is initially stored in the TE wave in the lower branch, has been transferred to the excitons of the WS_2 monolayer in the upper branch (see Figure S10 in the Supporting Information).

In our experiments, we used WS_2 monolayers with triangular shapes synthesized by using chemical vapor deposition and then transferred to the surface of the Si_3N_4/Ag heterostructure. The aqueous solution of PS nanoparticles was dropped on the WS_2 monolayer and dried naturally. The triangular WS_2 monolayers could be identified readily in the bright- and dark-field microscope images, as shown in **Figure 4**a. The PS nanoparticles located on the WS_2 monolayer could also be revealed in the corresponding dark-field image. In order to evaluate the damping rate of the nanocavity, we have experimentally measured the scattering spectra of a PS nanoparticle on the Si_3N_4 layer at different incidence angles, as shown in Figure 4b. Similar to the narrow resonances observed in the angle-resolved reflection spectra (see Figure 3b), one can see scattering peaks with linewidths as narrow as ≈43 and ≈66 meV at X_A and X_B, respectively. The photon–exciton coupling can be revealed by using the angle-resolved scattering spectra of the nanoparticle, as shown in Figure 4c,d. In each case, a scattering dip, which is independent of the incidence angle, is observed at the exciton resonance. The interaction between the TE wave and the two excitons in the WS_2 monolayer exhibits typical anticrossing behaviors. Benefiting from the narrow linewidth of the TE wave, the color change of the scattering light can be clearly observed by using *s*-polarized light with different incidence angles, shown in the inset of Figure 4c,d.

In **Figure 5**a, we present the energy dependences of the hybrid states (i.e., polaritons), which are referred to as the lower polariton (LP), middle polariton (MP), and upper polariton (UP) branches, extracted from the angle-resolved scattering spectra of the PS nanoparticle placed on the WS_2/Si_3N_4/Ag heterostructure. Anticrossing behaviors are clearly observed at the two exciton resonances. The energy dependences of the LP, MP and

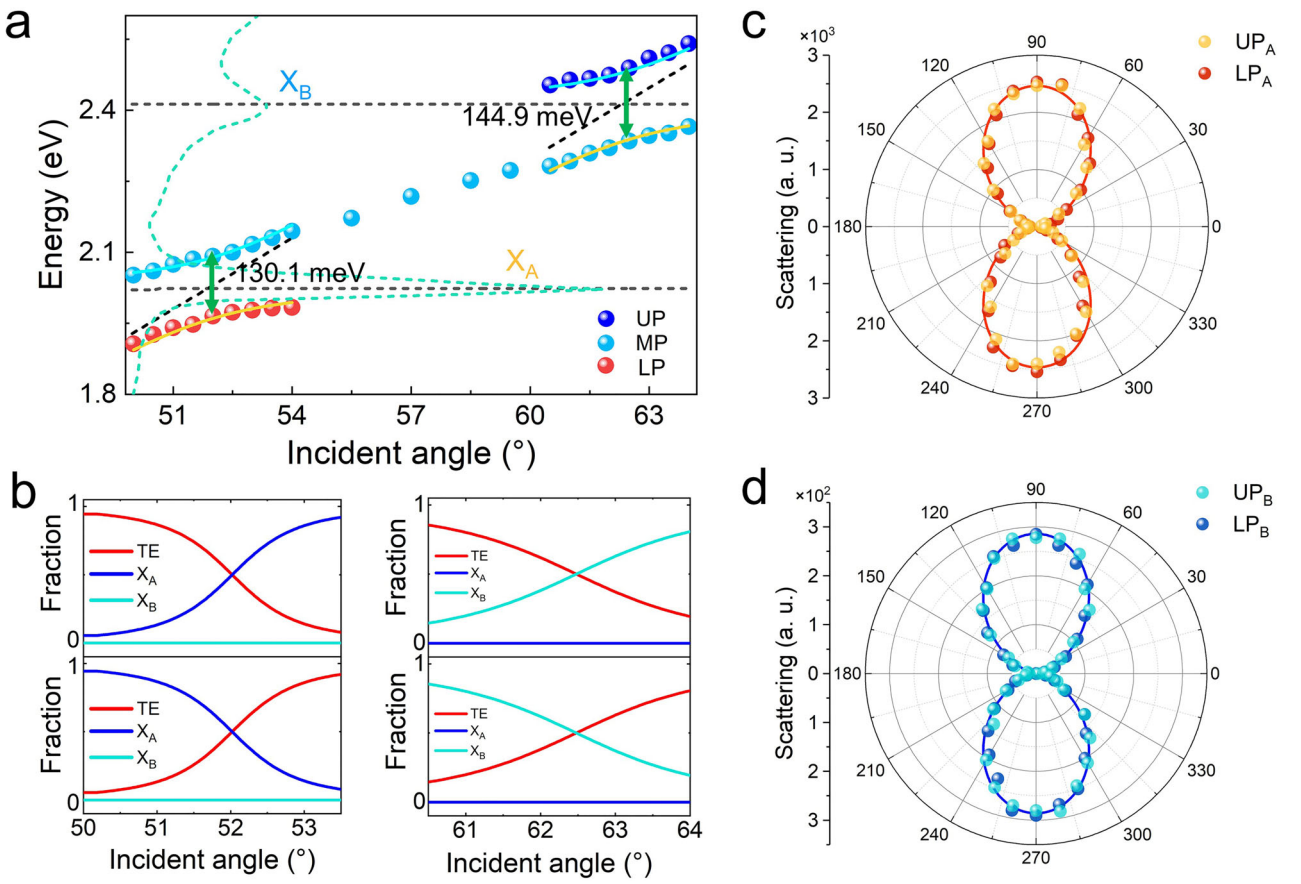

Figure 5. a) LP, MP, and UP branches (solid symbols) extracted from the angle-resolved scattering spectra measured for the PS nanoparticle placed on the $WS_2/Si_3N_4/Ag$ heterostructure. The fittings of the experimental data based on the coupled harmonic oscillator model (solid curves) are also provided. The dashed lines indicate the eigenenergies of the TE wave and the two excitons (X_A and X_B) in the absence of coupling. b) Fractions of the TE wave and the two excitons (X_A and X_B) in the LP, MP, and UP branches. c) Dependence of the scattering intensity on the polarization angle obtained for the hybrid states of the TE wave and X_A (i.e., the LP and MP branches) at zero detuning ($\lambda = 631.5$ nm and $\lambda = 592.2$ nm). d) Dependence of the scattering intensity on the polarization angle obtained for the hybrid states of the TE wave and X_B (i.e., the MP and UP branches) at zero detuning ($\lambda = 531.7$ nm and $\lambda = 500.6$ nm).

UP branches were fitted by using the coupled harmonic oscillator model based on a 3×3 Hamiltonian described in Equation (6), as shown by the solid curves in Figure 5a. The eigenenergies of the TE wave and the two exciton resonances are indicated by dashed lines. When the detuning energy between the TE wave and the exciton resonance (X_A or X_B) is equal to zero, the energy difference between the LP and MP (or the MP and UP) gives the Rabi splitting energy. The Rabi splitting energies were found to be ≈130.1 and ≈144.9 meV for X_A and X_B, respectively. In both cases, the Rabi splitting energy is much larger than the average damping rate of photons and excitons (≈38 meV at X_A and ≈73 meV at X_B), implying that the photon–exciton coupling in both cases enters undoubtedly into the strong-coupling regime. We also calculated the fractions of the TE wave and the two exciton resonances in the LP, MP, and UP branches, as shown in Figure 5b. Owing to the decoupling between the two exciton resonances, X_B is not found in the LP branch while X_A is not observed in the UP branch. It should be emphasized, however, that the hybridization of the three excitations (i.e., TE, X_A, and X_B), which is similar to the phenomenon reported previously,[38] may occur if the coupling strength between the TE wave and the two exciton resonances can be further improved. To gain a deep insight into the two polaritons propagating in the $WS_2/Si_3N_4/Ag$ heterostructure, we employed a polarization analyzer, which was inserted in the collection channel, to characterize the polarization of the scattering light from the hybrid states of the TE wave and the two excitons (i.e., the two polariton states), as shown in Figure 5c,d. In each case, we measured the polarization-dependent scattering intensity at the two hybrid states formed at zero detuning. Surprisingly, it was found that the two polaritons are linearly polarized along the *y*-direction (or TE-polarized), which is the same as that of the excitation light (i.e., *s*-polarized). To the best of our knowledge, this is the first demonstration of propagating polaritons with distinct polarization, which implies potential applications in wavelength conversion and quantum information.

3. Conclusions

In summary, we have investigated the photon–exciton coupling induced by the TE wave propagating in a Si_3N_4/Ag heterostructure and excitons (X_A and X_B) in a WS_2 monolayer. It was found that the spatial separation between the electric and magnetic

fields in the TE wave leads to small damping rates and narrow linewidths, which are comparable to those of the two exciton resonances. By using a PS nanoparticle as a scatter, the strong coupling between the TE waves and the two excitons is simultaneously revealed as anticrossing behaviors in the angle-resolved scattering spectra. The strong photon–exciton coupling was confirmed by the large Rabi splitting, which were found to be ≈130.1 and ≈144.9 meV for X_A and X_B, respectively. Our findings open new horizons for light–matter interaction by utilizing surface plasmon waves with small damping rates and pave the way for constructing plasmonic devices by exploiting dielectric-metal heterostructures and 2D materials.

4. Experimental Section

Sample Fabrication: The $WS_2/Si_3N_4/Ag$ heterostructure used in this work was fabricated by the following procedure. First, an Ag film with a thickness of 50 nm was coated on a SiO_2 substrate by using electron bean evaporation. Then, a Si_3N_4 layer with a thickness of 100 nm was deposited on the Ag film via high-frequency plasma-enhanced chemical vapor deposition (HF-PECVD). The thickness of the Si_3N_4 layer was controlled by the deposition time. The thickness and optical constant of the Si_3N_4 layer were measured by using an ellipsometer. The WS_2 monolayers were first synthesized on a Si substrate via chemical vapor deposition and then transferred to a Si_3N_4/Ag heterostructure, forming $WS_2/Si_3N_4/Ag$. The aqueous solution of PS nanospheres was dropped on the $WS_2/Si_3N_4/Ag$ heterostructure and dried naturally.

Optical Characterization: The TE and TM waves supported by the Si_3N_4/Ag heterostructure could be excited via the so-called Kretschmann–Raether configuration, as schematically shown in Figure 1a. The sample was mounted on a prism made of SiO_2 (K9 glass) with silicone oil whose refractive index was close to that of SiO_2. The *s*- or *p*-polarized white light was coupled into the Si_3N_4/Ag heterostructure by exploiting the total internal reflection occurring at the surface of the prism when the incidence angle exceeds the critical value (i.e., $\theta > \theta_c \approx 43°$). The dark-field images and scattering spectra of the PS nanoparticle placed on the $WS_2/Si_3N_4/Ag$ heterostructure were characterized by using an inverted microscope (Axio Observer A1, Zeiss) equipped with a spectrometer (SR-500i-B1, Andor) and a color charge coupled device (CCD) (DS-Ri2, Nikon). A polarization analyzer was inserted in the collection channel to examine the polarization of the scattering light.

Numerical Simulation: The reflectance spectra of $WS_2/Si_3N_4/Ag$ and $Si_3N_4/WS_2/Ag$ heterostructures and the scattering spectra of the PS nanoparticle placed on the surface of the $WS_2/Si_3N_4/Ag$ heterostructure were calculated numerically by using the finite-difference time-domain (FDTD) method (FDTD solution, https://www.lumerical.com). The refractive index of Si_3N_4 was based on the measured data while the dielectric constants of Ag and WS_2 monolayer were taken from literature.[50,51] The X_A and X_B exciton energies in WS_2 monolayer were chosen to be 2.02 and 2.41 eV, respectively. The thickness of the WS_2 monolayer was set to be 1.0 nm. The smallest mesh size was chosen to be 0.5 nm in order to obtain converged simulation results, and perfectly matched layer boundary condition was employed to terminate the finite simulation region.

Supporting Information

Supporting Information is available from the Wiley Online Library or from the author.

Acknowledgements

S.L. and L.Z. contributed equally to this work. S.L. acknowledged the financial support from the National Key Research and Development Program of China (Program No. 2016YFA0201002), the National Natural Science Foundation of China (Grant Nos. 11674110 and 11874020), and the Science and Technology Program of Guangzhou (Program No. 2019050001).

Conflict of Interest

The authors declare no conflict of interest.

Data Availability Statement

The data that support the findings of this study are available from the corresponding author upon reasonable request.

Keywords

2D materials, dielectric-metal heterostructures, strong coupling, transverse-electric polarized waves

Received: August 17, 2021
Revised: June 3, 2022
Published online:

[1] E. Cao, W. Lin, M. Sun, W. Liang, Y. Song, *Nanophotonics* **2018**, *7*, 145.
[2] A. F. Kockum, A. Miranowicz, S. De Liberato, S. Savasta, F. Nori, *Nat. Rev. Phys.* **2019**, *1*, 19.
[3] H. Groß, J. M. Hamm, T. Tufarelli, O. Hess, B. Hecht, *Sci. Adv.* **2018**, *4*, eaar4906.
[4] K. Hennessy, A. Badolato, M. Winger, D. Gerace, M. Atatüre, S. Gulde, S. Fält, E. L. Hu, A. Imamoğlu, *Nature* **2007**, *445*, 896.
[5] P. Vasa, R. Pomraenke, G. Cirmi, E. De Re, W. Wang, S. Schwieger, D. Leipold, E. Runge, G. Cerullo, C. Lienau, *ACS Nano* **2010**, *4*, 7559.
[6] T. Volz, A. Reinhard, M. Winger, A. Badolato, K. J. Hennessy, E. L. Hu, A. Imamoğlu, *Nat. Photonics* **2012**, *6*, 605.
[7] M. Lončar, T. Yoshie, A. Scherer, P. Gogna, Y. Qiu, *Appl. Phys. Lett.* **2002**, *81*, 2680.
[8] S. K. Rajendran, M. Wei, H. Ohadi, A. Ruseckas, G. A. Turnbull, I. D. Samuel, *Adv. Opt. Mater.* **2019**, *7*, 1801791.
[9] S. Christopoulos, G. B. H. Von Högersthal, A. Grundy, P. Lagoudakis, A. Kavokin, J. Baumberg, G. Christmann, R. Butté, E. Feltin, J.-F. Carlin, N. Grandjean, *Phys. Rev. Lett.* **2007**, *98*, 126405.
[10] R. Liu, Z.-K. Zhou, Y.-C. Yu, T. Zhang, H. Wang, G. Liu, Y. Wei, H. Chen, X.-H. Wang, *Phys. Rev. Lett.* **2017**, *118*, 237401.
[11] O. Bitton, S. N. Gupta, G. Haran, *Nanophotonics* **2019**, *8*, 559.
[12] M. Pelton, M. Sheldon, J. Khurgin, *Nanophotonics* **2019**, *8*, 513.
[13] R. Chikkaraddy, B. De Nijs, F. Benz, S. J. Barrow, O. A. Scherman, E. Rosta, A. Demetriadou, P. Fox, O. Hess, J. J. Baumberg, *Nature* **2016**, *535*, 127.
[14] N. T. Fofang, T.-H. Park, O. Neumann, N. A. Mirin, P. Nordlander, N. J. Halas, *Nano Lett.* **2008**, *8*, 3481.
[15] N. T. Fofang, N. K. Grady, Z. Fan, A. O. Govorov, N. J. Halas, *Nano Lett.* **2011**, *11*, 1556.
[16] A. Manjavacas, F. J. García de Abajo, P. Nordlander, *Nano Lett.* **2011**, *11*, 2318.
[17] E. Kretschmann, H. Raether, *Z. Naturforsch., A: Phys. Sci.* **1968**, *23*, 2135.
[18] A. V. Zayats, I. I. Smolyaninov, A. A. Maradudin, *Phys. Rep.* **2005**, *408*, 131.

[19] P. Törmä, W. L. Barnes, *Rep. Prog. Phys.* **2014**, *78*, 013901.
[20] J. Huang, G. M. Akselrod, T. Ming, J. Kong, M. H. Mikkelsen, *ACS Photonics* **2018**, *5*, 552.
[21] F. Deng, H. Liu, L. Xu, S. Lan, A. E. Miroshnichenko, *Laser Photonics Rev.* **2020**, *14*, 1900420.
[22] H. Zhang, *ACS Nano* **2015**, *9*, 9451.
[23] X. Duan, C. Wang, A. Pan, R. Yu, X. Duan, *Chem. Soc. Rev.* **2015**, *44*, 8859.
[24] X. Li, L. Zhou, Z. Hao, Q. Q. Wang, *Adv. Opt. Mater.* **2018**, *6*, 1800275.
[25] M. Chhowalla, H. S. Shin, G. Eda, L.-J. Li, K. P. Loh, H. Zhang, *Nat. Chem.* **2013**, *5*, 263.
[26] X. Zhang, X. Zhang, W. Huang, K. Wu, M. Zhao, A. Charlie Johnson, S. Tongay, E. Cubukcu, *Adv. Opt. Mater.* **2020**, *8*, 1901988.
[27] H. Huang, F. Deng, J. Xiang, S. Li, S. Lan, *Appl. Surf. Sci.* **2021**, *542*, 148660.
[28] Y. B. Zheng, B. K. Juluri, L. L. Jensen, D. Ahmed, M. Lu, L. Jensen, T. J. Huang, *Adv. Mater.* **2010**, *22*, 3603.
[29] J. Sun, H. Hu, D. Zheng, D. Zhang, Q. Deng, S. Zhang, H. Xu, *ACS Nano* **2018**, *12*, 10393.
[30] R.-Q. Li, F. García-Vidal, A. Fernández-Domínguez, *ACS Photonics* **2018**, *5*, 177.
[31] H. Wang, J. Wen, W. Wang, N. Xu, P. Liu, J. Yan, H. Chen, S. Deng, *ACS Nano* **2019**, *13*, 1739.
[32] X. Yu, Y. Yuan, J. Xu, K. T. Yong, J. Qu, J. Song, *Laser Photonics Rev.* **2019**, *13*, 1800219.
[33] Z. Cai, Y. Xu, C. Wang, Y. Liu, *Adv. Opt. Mater.* **2020**, *8*, 1901090.
[34] X. Han, K. Wang, X. Xing, M. Wang, P. Lu, *ACS Photonics* **2018**, *5*, 3970.
[35] J. Cuadra, D. G. Baranov, M. Wersall, R. Verre, T. J. Antosiewicz, T. Shegai, *Nano Lett.* **2018**, *18*, 1777.
[36] K. F. Mak, J. Shan, *Nat. Photonics* **2016**, *10*, 216.
[37] A. Boulesbaa, B. Huang, K. Wang, M.-W. Lin, M. Mahjouri-Samani, C. Rouleau, K. Xiao, M. Yoon, B. Sumpter, A. Puretzky, D. Geohegan, *Phys. Rev. B* **2015**, *92*, 115443.
[38] A. H. Rose, J. R. Dunklin, H. Zhang, J. M. Merlo, J. van de Lagemaat, *ACS Photonics* **2020**, *7*, 1129.
[39] H.-Z. Chen, T. Liu, H.-Y. Luan, R.-J. Liu, X.-Y. Wang, X.-F. Zhu, Y.-B. Li, Z.-M. Gu, S.-J. Liang, H. Gao, L. Lu, L. Ge, S. Zhang, J. Zhu, R.-M. Ma, *Nat. Phys.* **2020**, *16*, 571.
[40] G. Khitrova, H. Gibbs, M. Kira, S. W. Koch, A. Scherer, *Nat. Phys.* **2006**, *2*, 81.
[41] Y. Sang, C.-Y. Wang, S. S. Raja, C.-W. Cheng, C.-T. Huang, C.-A. Chen, X.-Q. Zhang, H. Ahn, C.-K. Shih, Y.-H. Lee, J. Shi, S. Gwo, *Nano Lett.* **2021**, *21*, 2596.
[42] S. Li, L. Zhou, M. Panmai, J. Xiang, S. Lan, *Nanophotonics* **2021**, *10*, 2639.
[43] G. T. Papadakis, D. Fleischman, A. Davoyan, P. Yeh, H. A. Atwater, *Nat. Commun.* **2018**, *9*, 296.
[44] N. C. Passler, A. Heßler, M. Wuttig, T. Taubner, A. Paarmann, *Adv. Opt. Mater.* **2020**, *8*, 1901056.
[45] T. F. Krauss, *J. Phys. D: Appl. Phys.* **2007**, *40*, 2666.
[46] S. Lan, S. Nishikawa, O. Wada, *Appl. Phys. Lett.* **2001**, *78*, 2101.
[47] D. Zheng, S. Zhang, Q. Deng, M. Kang, P. Nordlander, H. Xu, *Nano Lett.* **2017**, *17*, 3809.
[48] J. Wen, H. Wang, W. Wang, Z. Deng, C. Zhuang, Y. Zhang, F. Liu, J. She, J. Chen, H. Chen, *Nano Lett.* **2017**, *17*, 4689.
[49] P. Gonçalves, L. Bertelsen, S. Xiao, N. A. Mortensen, *Phys. Rev. B* **2018**, *97*, 041402.
[50] P. B. Johnson, R.-W. Christy, *Phys. Rev. B* **1972**, *6*, 4370.
[51] Y. Li, A. Chernikov, X. Zhang, A. Rigosi, H. M. Hill, A. M. Van Der Zande, D. A. Chenet, E.-M. Shih, J. Hone, T. F. Heinz, *Phys. Rev. B* **2014**, *90*, 205422.